RESEARCH ARTICLE

Surface temperature comparison of the Arctic winter MOSAiC observations, ERA5 reanalysis, and MODIS satellite retrieval

Lia Herrmannsdörfer[1,*], Malte Müller[1,2], Matthew D. Shupe[3,4], and Philip Rostosky[5]

Atmospheric model systems, such as those used for weather forecast and reanalysis production, often have significant and systematic errors in their representation of the Arctic surface energy budget and its components. The newly available observation data of the Multidisciplinary drifting Observatory for the Study of Arctic Climate (MOSAiC) expedition (2019/2020) enable a range of model analyses and validation in order to advance our understanding of potential model deficiencies. In the present study, we analyze deficiencies in the surface radiative energy budget over Arctic sea ice in the ERA5 global atmospheric reanalysis by comparing against the winter MOSAiC campaign data, as well as, a pan-Arctic level-2 MODIS ice surface temperature remote sensing product. We find that ERA5 can simulate the timing of radiatively clear periods, though it is not able to distinguish the two observed radiative Arctic winter states, radiatively clear and opaquely cloudy, in the distribution of the net surface radiative budget. The ERA5 *surface temperature* over Arctic sea ice has a conditional error with a positive bias in radiatively clear conditions and a negative bias in opaquely cloudy conditions. The mean surface temperature error is 4°C for radiatively clear situations at MOSAiC and up to 15°C in some parts of the Arctic. The spatial variability of the surface temperature, given by 4 observation sites at MOSAiC, is not captured by ERA5 due to its spatial resolution but represented in the level-2 satellite product. The sensitivity analysis of possible error sources, using satellite products of *snow depth* and *sea ice thickness*, shows that the positive surface temperature errors during radiatively clear events are, to a large extent, caused by insufficient sea ice thickness and snow depth representation in the reanalysis system. A positive bias characterizes regions with ice thickness greater than 1.5 m, while the negative bias for thinner ice is partly compensated by the effect of snow.

Keywords: Surface temperature, Energy budget, Arctic, Sea ice, ERA5, MOSAiC

Introduction

The Earth's energy budget is determined by the incoming solar radiation, which is distributed unevenly over the curved surface. The induced imbalance between polar and equatorial regions causes a poleward atmospheric energy transport (Serreze and Barry, 2014). In the Arctic, a net energy loss to space dominates and the surface energy budget plays an essential role in its determination. The strongest net loss of energy occurs during the polar night, when shortwave radiation is negligible and longwave

radiation, sensible, latent, and conductive heat fluxes control the surface energy budget (Peixoto and Oort, 1992).

In the sea ice–covered Arctic, the net longwave radiation is, on the one hand, strongly dependent on atmospheric characteristics, such as air temperature, moisture, and the presence of clouds (Zhang et al., 1996; Stramler et al., 2011). On the other hand, the thickness of the combined sea ice and snow layer plays an important role due to its insulation of the relatively warm ocean, at around −2°C, from the cold atmosphere (Overland and Guest, 1991). In other words, the net longwave radiation consists of radiation emitted downward, from the atmosphere into the ice surface, and upward, from the ice surface into the atmosphere (Serreze and Barry, 2014). When liquid and mixed-phase clouds are present (opaquely cloudy state), the surface and cloudy atmosphere are in near radiative equilibrium with the downward atmospheric and upward surface emission in approximate balance. In the absence of (optically thick) clouds (radiatively clear state), longwave radiation emitted downward from the atmosphere is decreased, resulting in a strongly negative radiative energy budget at the surface

[1] Development Centre for Weather Forecasting, Norwegian Meteorological Institute, Oslo, Norway

[2] Department of Geosciences, University of Oslo, Oslo, Norway

[3] Cooperative Institute for Research in Environmental Science, University of Colorado, Boulder, CO, USA

[4] NOAA/Physical Sciences Laboratory, Boulder, CO, USA

[5] Institute of Environmental Physics, University of Bremen, Bremen, Germany

* Corresponding author:
Email: lia.f.herrmannsdoerfer@gmail.com

and, thus, the highest energy loss. Thin ice clouds with a high cloud base, such as cirrus clouds, do not typically affect the surface energy budget significantly and, thus, can be present in radiatively clear conditions (Graham et al., 2017). The temperature of the sea ice surface is to a large extent controlled by the surface radiative energy budget. Hence, the Arctic winter atmosphere is predominantly found in these two radiative states and related surface temperatures, which are driven by the presence or absence of optically thick clouds (Zhang et al., 1996; Shupe and Intrieri, 2004; Stramler et al., 2011; Graham et al., 2017; Walden et al., 2017).

Due to its importance for the global climate system, as well as for local processes, an accurate representation of the Arctic energy budget in global and regional Earth system models, weather forecasts, and reanalyses is important (Sorteberg et al., 2007; Tjernström and Graversen, 2009; Jakobson et al., 2012; Lindsay et al., 2014). Specifically, it is highly relevant to understand potential deficiencies in model systems that are used for reanalyses production, since those products are often used for model evaluations or process understanding. One of the newest global reanalyses is ERA5 with a horizontal resolution of about 31 km (Hersbach et al., 2020). Previous studies showed that the model predecessor ERA-Interim does not sufficiently represent the surface energy budget, atmospheric boundary layer, cloud properties, and sea ice concentration, which is partly also inherited to the ERA5 atmospheric reanalysis (Graham et al., 2017; Kayser et al., 2017; Graham et al., 2019; Wang et al., 2019; Renfrew et al., 2021; Arduini et al., 2022). Another important error source is the parameterization of Arctic sea ice with constant thickness and without snow (European Centre for Medium-Range Weather Forecasts [ECMWF], 2016; Batrak and Müller, 2019; Wang et al., 2019; Arduini et al., 2022). Previous studies found a warm bias of 2m-air temperature (T2M) and surface temperature (T_s) for the ERA5 reanalysis in the sea ice–covered Arctic. Largest biases were found during cold winter conditions with errors of about 5°C for T2M lower than −25°C (Wang et al., 2019), and especially in radiatively clear winter periods with T_s errors of up to 15°C (Batrak and Müller, 2019). Smaller T2M errors of 2°C–3°C are found along the Marginal Ice Zone of the Greenland Sea (Renfrew et al., 2021) and in the Central Arctic (Krumpen et al., 2021).

Since conventional observations of the Central Arctic are sparse, expeditions are crucial for understanding the Arctic system and improving models in the Arctic domain. Scientific expeditions offer a wide range of interdisciplinary observations. Examples are the *Surface Heat Budget of the Arctic Ocean* (SHEBA) expedition (1997/1998; Uttal et al., 2002) and the *Norwegian Young Sea Ice* (N-ICE2015) expedition (2015; Cohen et al., 2017). The recent *Multidisciplinary drifting Observatory for the Study of Arctic Climate* (MOSAiC, 2019/2020) expedition has provided a unique data set with which to understand the components of the Arctic System, their interactions, and their spatial variability and heterogeneity at multiple scales and during the seasonal cycle (Shupe et al., 2020).

In addition to expeditions, which are restricted to certain regions, satellite observations allow for a spatially coherent view and can help to set point measurements into a large-scale context. For example, the MODIS spectroradiometer onboard Aqua and Terra satellites offers a wide range of observations of the Earth's surface and the atmosphere with a high spatial and temporal resolution in the Arctic (Hall et al., 2004; Hall and Riggs, 2015). As another example, surface and subsurface measurements of CryoSat-2, Soil Moisture and Ocean Salinity (SMOS), and Advanced Microwave Scanning Radiometer (AMSR-E/AMSR-2) can be used to derive variables such as sea ice thickness or snow depth for most of the Arctic, which cannot be gathered from in situ observations with sufficient coverage (Ricker et al., 2017; Rostosky et al., 2018).

In the present study, the ERA5 global atmospheric reanalysis representation of the surface longwave radiation and surface temperature in the sea ice–covered Arctic is analyzed for the MOSAiC expedition winter 2019/2020. The surface longwave radiation in ERA5 is assessed for the ability to simulate the radiative states. The surface temperature in ERA5 is compared to MOSAiC and MODIS observations, along the MOSAiC drift trajectory and in a pan-Arctic context. A particular focus is set on the representation of radiatively clear conditions, as well as on the reanalysis model system's deficiencies in describing the sea ice and snow cover and the impact on the surface temperature representation.

Data
ERA5 reanalysis
The ERA5 reanalysis is a widely used global atmospheric reanalysis, provided by ECMWF, covering the time period of 1950 until present at a horizontal resolution of 31 km. A wide range of conventional and nonconventional observations (e.g., synoptic stations, drifting buoys, air planes, radiosondes, and satellites) are assimilated in the coupled atmospheric and surface models. In the Arctic ocean, prescribed sea ice concentration (CI) defines tiles as surface type, ice or water. Sea ice is simulated with 4 layers, adding up to a constant 1.5 m ice thickness. The Arctic ocean and atmosphere act as lower and upper boundary layers to the sea ice, with prescribed sea surface temperature (−1.7°C) and surface skin temperature (SKT) in balance with the surface fluxes. There is no representation of change in conductive heat flux due to snow on sea ice (ECMWF, 2016; Hersbach et al., 2020). In this study, surface longwave radiative fluxes and SKT are analyzed (see Methods section for more details).

MOSAiC surface measurements
MOSAiC was a yearlong international and interdisciplinary expedition from autumn 2019 to autumn 2020. The icebreaker Polarstern (Knust, 2017) drifted with the sea ice, from the Laptev Sea, through the Central Arctic and into the Fram Strait (**Figure 1a**). Measurements of various components of the Arctic system and their interaction (e.g., thermodynamic structure of the lower atmosphere, aerosols, ice morphology, ocean turbulence) were carried
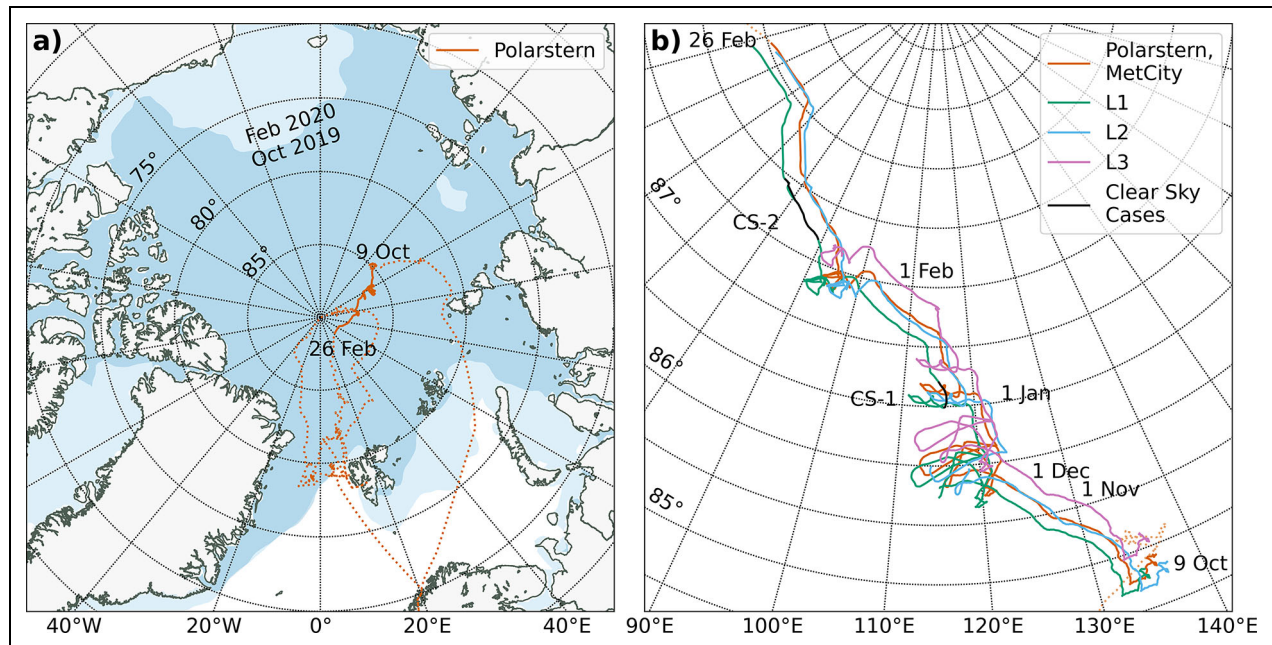
Figure 1. Trajectory of the MOSAiC drift campaign. (a) Trajectory of the research vessel Polarstern (orange) during the MOSAiC drift campaign from autumn 2019 to autumn 2020 with areas of sea ice concentration >20% in October 2019 and February 2020. (b) Trajectory of Polarstern with nearby Central Observatory Met City, and L-sites at the Distributed Network (L1 green, L2 blue, and L3 purple) during the analyzed period from October 9, 2019, to February 26, 2020, and the clear sky periods CS-1 and CS-2 (black). MOSAiC = Multidisciplinary drifting Observatory for the Study of Arctic Climate.

out at multiple spatial scales and covering the seasonal cycle of a full year (Shupe et al., 2020). In this study, the surface broadband longwave radiative fluxes and surface temperature, based on surface broadband longwave radiometric emission assuming a surface emissivity of 0.98, are used. The individual measurement errors are small relative to the spatial variability of these parameters across the grid resolution of the reanalysis product. The error of the surface broadband longwave temperature due to assuming constant emissivity is estimated to be 0.04°C for the MOSAiC winter. The central set of observations are from the Met City at the MOSAiC Central Observatory (CO; Cox et al., 2021d), close to the research vessel Polarstern, which served as the centrepiece of the expedition (**Figure 1b**). In addition, observations from the Atmospheric Surface Flux Stations (ASFS) positioned at the L1, L2, and L3 sites in the MOSAiC Distributed Network around the research vessel are used (Cox et al., 2021a; Cox et al., 2021b; Cox et al., 2021c). The positions of the sites L1, L2, and L3, relative to the research vessel, change slightly due to ice deformation, with an average distance of 16 km (L1), 10 km (L2), and 23 km (L3). The distances between the observational sites range from 11 km to 34 km (**Figure 2**).

MODIS ice surface temperature
MODIS ice surface temperature is retrieved from the *Moderate Resolution Imaging Spectroradiometer* onboard of the satellites Terra and Aqua, from visible and near-infrared brightness temperature observations, during day and night, and for cloud-free ocean grid cells. Error sources are the false distinction of cloud tops from the ice surface

for low winter temperatures, a too conservative cloud filter, and limited representativity of the coefficients used for deriving surface temperatures from brightness temperatures. A bias of -21°C and root mean square error (RMSE) of 3.7°C were derived for Arctic winter conditions, which can be decreased significantly by additional cloud filtering (Hall et al., 2004; Hall and Riggs, 2015).

CryoSat-2/SMOS sea ice thickness
CryoSat-2/SMOS sea ice thickness (h_i) is a weekly composite of sea ice thicknesses based on CryoSat-2 altimeter ice freeboard estimates and SMOS microwave radiometer brightness temperature at L-Band. Due to the complementary sensitivity of the CryoSat-2 and SMOS methods for different sea ice thickness regimes, the overall uncertainty of the combined product is decreased (Ricker et al., 2017). Errors result from assumed snow properties and depth, sea ice concentration <100% (SMOS) and the measurability of thick, heavily deformed multiyear ice (MYI). The product uncertainty is given with 0–1 m and is highest on MYI (Ricker et al., 2017). The used product is shown in **Figure 3**.

AMSR-E/2 snow depth
AMSR-E/2 snow depth (h_s) is deduced daily by relating AMSR-E and AMSR-2 brightness temperature to snow observations over first-year ice (FYI) and MYI. Main sources of uncertainty are the limited size of training data sets and high spatial variability of snow and ice thickness in MYI regions. Average uncertainties are 0.1–6 cm for FYI and 3.4–9.4 cm for MYI (Rostosky et al., 2018). Comparison to the MOSAiC in situ observations showed good agreement
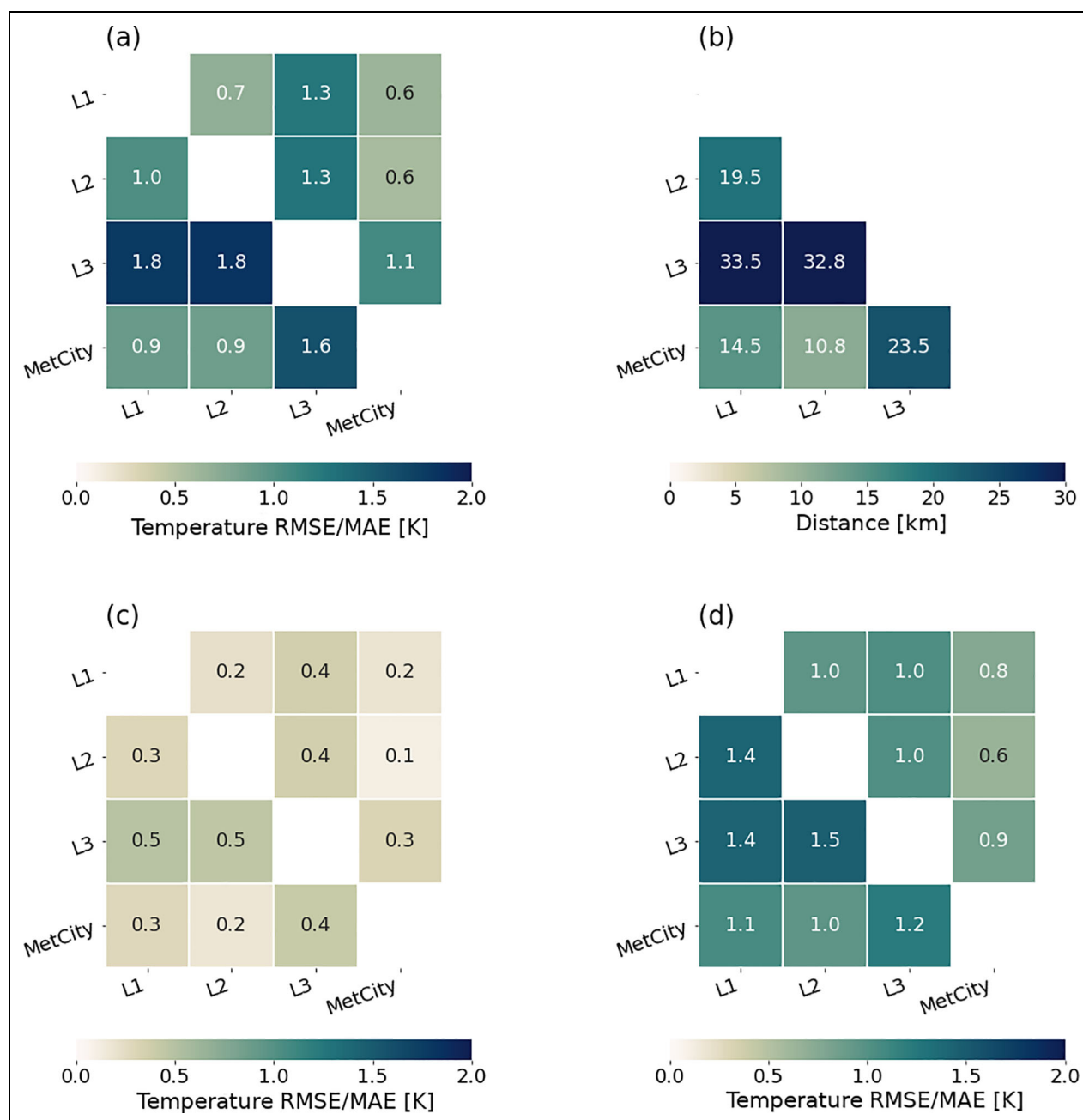
Figure 2. Variability between the different observation sites. The mean distance and surface temperature variability between the 4 observation station locations (L1, L2, L3, and Met City). In (a), (c), and (d), the mean absolute error (upper right triangle) and root mean square error (lower left triangle) of the surface temperature between the different locations are shown. In (a) for the in situ observations, (c) for the ERA5 reanalysis, and (d) for the MODIS satellite observations. In (b) the mean distance between the stations is shown.

within a 5 cm uncertainty (Krumpen et al., 2021). The applicability is limited due to the seasonal evolution of snow conditions and sensitivity of the used wave lengths on the different snow conditions. Over MYI, snow is only retrieved in March and April due to an ambiguous microwave signal of snow and MYI, which is especially pronounced during early winter (Rostosky et al., 2018). The used product is shown in **Figure 3**.

OSI-SAF sea ice concentration
Processed sea ice concentration (CI) satellite observations from *Ocean and Sea Ice Satellite Application Facilities* (OSI-

SAF) are used in this study. The used product is shown in **Figure 3**. Note that ERA5 uses a perturbed version of the operational OSI-SAF sea ice concentration (Hersbach et al., 2020).

Methods
We utilize the MOSAiC observations of the time period from October 9, 2019, to February 26, 2020. During the entire period, the shortwave radiation is negligible at MOSAiC. For the pan-Arctic analysis, we use a winter time period from November 1, 2019, to February 28, 2020, when shortwave radiation is insignificant north of 70°N, which includes most of the sea ice–covered Arctic. In
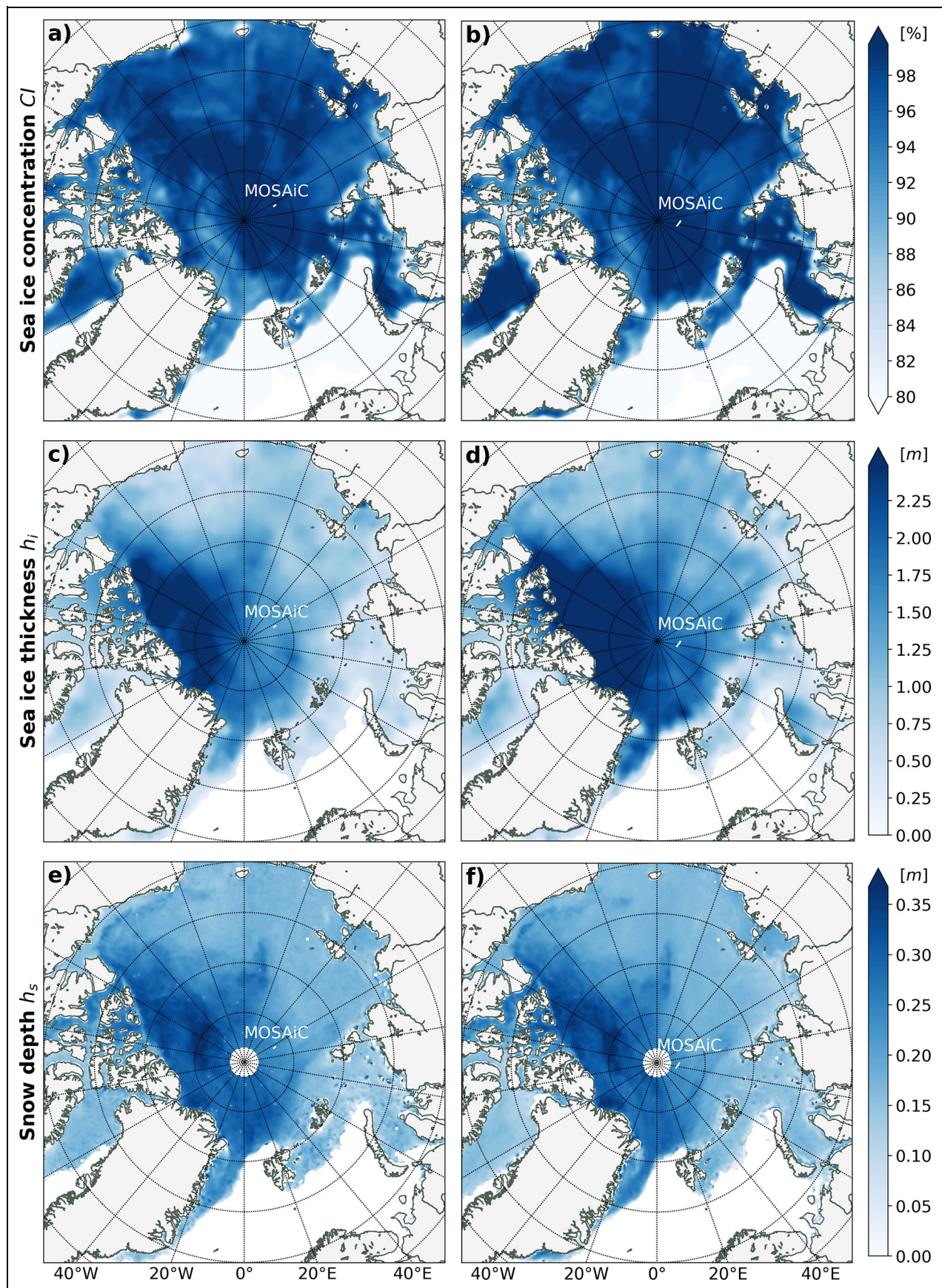
Figure 3. Pan-Arctic conditions of snow and sea ice. Satellite observations of the *sea ice concentration* (CI, %) $\geq 80\%$ from OSI-SAF (first row), *sea ice thickness* (h_i, m) from CryoSat-2/SMOS (second row), and *snow depth* (h_s, m) from AMSR-E/2 (third row). Averaged over the clear sky cases CS-1 (first column) and CS-2 (second column).

addition, the ERA5 data are filtered and only data are considered where the incoming shortwave radiation is zero.

In the following, these representative winter time periods are filtered for radiatively clear conditions. A detailed analysis is carried out for all radiatively clear conditions using hourly data during winter 2019/2020 (CS), for all radiatively clear conditions correctly simulated by ERA5 (hits) and for the 2 clear sky events CS-1 (0300 UTC, December 31, 2019, to 0400 UTC, January 2, 2020) and CS-2 (0500 UTC, February 10, 2020, to 1400 UTC, February 17, 2020). The CS-1 and CS-2 are the longest (consistent) radiatively clear winter periods at MOSAiC. During the analysis, these periods were confirmed as radiatively clear by a threshold of observed net longwave radiation (LWN < -35 W m^{-2}) and as largely cloud free by independent satellite observations. Thus, the periods can also be called clear sky. Temporal averages of CS-2 exclude time steps from 1500 UTC, February 13, 2020, to 1700 UTC, February 14, 2020, as they are largely influenced by cyclonic activity (Rinke et al., 2021). CS-1 and CS-2 show different characteristics of the atmospheric state and snow and ice conditions, enabling an analysis of the impact of different characteristics on the surface temperature error.

The analysis is carried out along the trajectory of the 4 MOSAiC observation sites during the given winter time (**Figure 1**). The MOSAiC track was characterized by high CI >98% during the analyzed time (Krumpen et al., 2021).

In addition to the comparison along the MOSAiC trajectory, the reanalysis is compared to the pan-Arctic satellite retrievals of sea ice surface temperature during polar night radiatively clear conditions. We limit the analysis to the sea ice–covered areas (CI > 20%) north of 70°N, where solar radiation is negligible (SW = 0 W m^{-2}) and optically thick clouds can be excluded by LWN(MOSAiC) < -35 W m^{-2} and MODIS cloud mask.

Our analysis is restricted to the surface longwave radiation budget and surface temperature. The surface longwave radiation is gathered directly from MOSAiC and ERA5. The surface temperature on sea ice is used as described in the following and is referred to as surface temperature (T_s).

MOSAiC and MODIS measure the temperature of the uppermost surface ($T_{s_{MOSAiC}}$ and $T_{s_{MODIS}}$), based on brightness temperature (see *MODIS ice surface temperature*) and surface longwave radiation (see *MOSAiC surface measurements*). MODIS observations are derived for both sea ice and water surfaces (Hall and Riggs, 2015), but limited to CI >20% in this work. The ASFS were placed on solid, snow covered sea ice with $h_i \approx 1.7$ m and $h_s = 9.1$ cm (ASFS40 at L1), $h_i \approx 1$ m and $h_s = 8.3$ cm (ASFS30 at L2), and $h_i \approx 0.3$ m and $h_s = 6.5$ cm (ASFS50 at L3) with a significant distance to open water. Heavy sea ice deformation caused damage of the measurement systems ASFS50 (February 5, 2020) and ASFS40 (February 27, 2020), terminating the data availability at the sites L1 and L3 for the rest of the winter.

ERA5 output includes 2 surface temperature variables, the (radiative) skin temperature and the ice surface temperature. They are related to the uppermost layer of sea ice

or ocean and the upper 0.07 m of the ice layer, respectively (ECMWF, 2016). Because in MOSAiC and MODIS, the ice surface temperature is measured from the above, we utilize, due to its similar characteristics, the ERA5 skin temperature, in the following referred to as $T_{s_{ERA5}}$. The difference between ERA5 skin temperature and ice surface temperature is relatively small, within $\pm 2°$C for the analyzed domain and time. All areas with CI <20% are excluded in this analysis.

The reanalysis variables are available hourly on a pan-Arctic 31-km grid and, further, are colocated with the nearest grid cell along the MOSAiC drift trajectory. Matching the ERA5 availability, full-hour time samples of the 10-min MOSAiC observations are used. MODIS passage swaths are used as hourly Arctic composites of 5-km resolution. Daily AMSR-E/2 snow depths (25 km) are averaged over all days within the clear sky periods CS-1 and CS-2, while weekly CryoSat-2/SMOS sea ice thickness (25 km) closest to CS-1 (January 2, 2020) and CS-2 (February 13, 2020) are used.

In the following analysis, we provide error estimates of the ERA5 reanalysis surface temperature over sea ice. First, $T_{s_{ERA5}}$ is compared to the observed values of the MOSAiC observatory and to $T_{s_{MODIS}}$, along the winter MOSAiC trajectory. The differences of these products, the error estimates, are described as $\Delta T_{s_{MOSAiC}}$ and $\Delta T_{s_{MODIStrack}}$, respectively. Second, $T_{s_{ERA5}}$ is compared to MODIS over the entire ice-covered Arctic ($\Delta T_{s_{MODIS, Arctic}}$), for all radiatively clear conditions in winter 2019/2020 (CS), as well as, for the cases CS-1 and CS-2. Third, a theoretical error of the surface temperature ($\Delta T_{s_{theo}}$) is calculated for the cases CS-1 and CS-2. The theoretical error quantifies the misrepresentation of conductive heat flux through the sea ice and snow layers based on their thickness misrepresentation. It is thereby assumed that the conductive heat flux change is balanced by the longwave radiation budget (Batrak and Müller, 2019). Note that the theoretical error excludes other error sources, such as misrepresentation of longwave radiation. $\Delta T_{s_{theo}}$ is quantified as in the following:

$$\alpha = \frac{k_i \cdot k_s}{k_s \cdot h_i + k_i \cdot h_s},$$

$$\alpha' = \frac{k_i \cdot k_s}{k_s \cdot (h_i + \Delta h_i) + k_i \cdot (h_s + \Delta h_s)}, \quad (1)$$

$$\Delta T_s = \frac{(\alpha' - \alpha)(T_s[K] - T_o[K])}{4 \cdot \varepsilon \cdot \sigma \cdot T_s[K]^3 - \alpha'},$$

where h_i and h_s are $h_{i,ERA5} = 1.5$m and $h_{s,ERA5} = 0$m. The model errors of the ice thickness and snow depth representation are Δh_i and Δh_s, respectively. Δh_i and Δh_s are estimated from the CryoSat-2/SMOS ice thickness retrieval (Ricker et al., 2017) and the AMSR-E/2-based snow depths (Rostosky et al., 2018), which are shown in **Figure 3**. We define the snow conductivity as $k_s = 0.31$ W m^{-1} K^{-1} and sea ice conductivity as $k_i = 2.1$ W m^{-1} K^{-1}, following Overland and Guest (1991) and ECMWF (2016). T_s and T_o are the model ice/snow and ocean surface temperatures in Kelvin, respectively, where T_o is assumed to be 271.15 K. σ is the Stefan–Boltzmann constant and ε is the
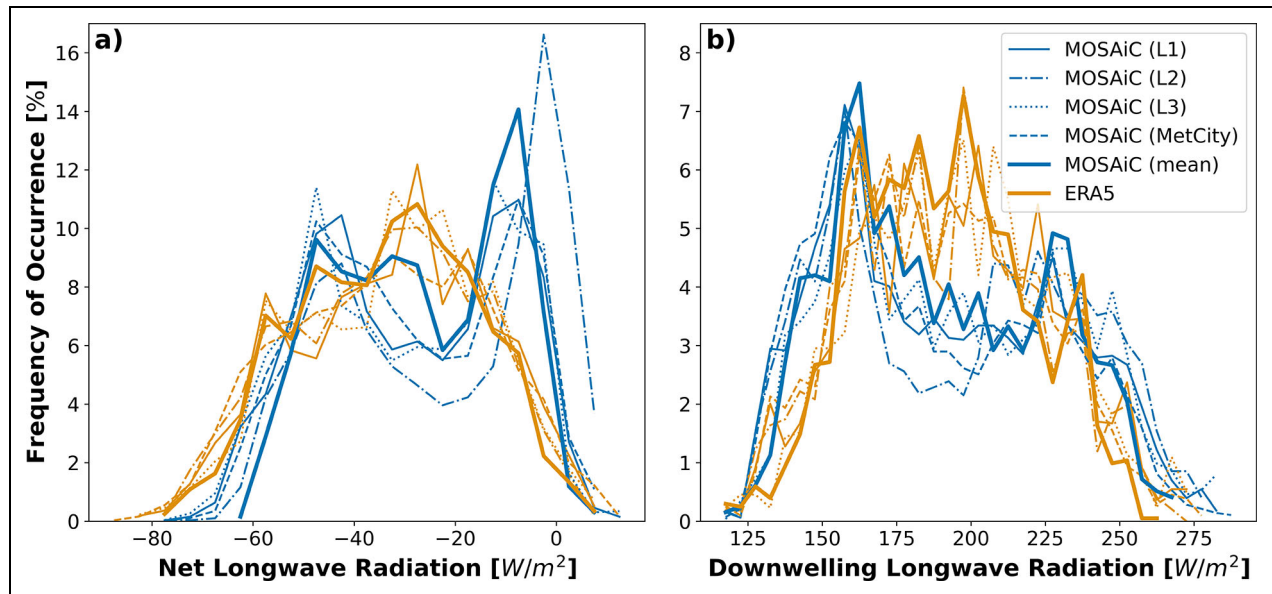
Figure 4. Surface longwave radiation. Surface (a) net and (b) downwelling longwave radiation [W m^{-2}] frequency of occurrence for MOSAiC observations (blue) and ERA5 reanalysis (orange) along the MOSAiC trajectory of the sites L1 (solid), L2 (dashed-dotted), L3 (dotted), Met City (dashed), and the mean of these sites (solid, thick) from October 9, 2019, to February 26, 2020. MOSAiC = Multidisciplinary drifting Observatory for the Study of Arctic Climate.

emissivity of the ice/snow surface and assumed to be 0.99. The sensitivity of the $\Delta T_{s_{theo.}}$ to Δh_i and Δh_s is analyzed by setting either Δh_s or Δh_i to 0 m, pretending the model had correct snow or sea ice representation.

The $\Delta T_{s_{theo.}}$ including a $\Delta h_i \neq 0$ is only calculated where $h_i \geq 1$ m, since Equation 1 is a first-order approximation of the temperature error and thus not valid for large deviations, caused by smaller sea ice thicknesses. $\Delta T_{s_{MODIS, Arctic}}$ and $\Delta T_{s_{theo.}}$ are filtered equally, with the conditions described above. Note the difference in between the error estimates $\Delta T_{s_{theo.}}$ and $\Delta T_{s_{MODIS}}$

Results
Determination of radiatively clear conditions for the MOSAiC winter 2019/2020 and representation by ERA5
MOSAiC winter observations of the surface net longwave radiation (LWN) range from -78 to $+17$ W m^{-2} at the MOSAiC sites with highest frequencies of occurrence at around -7 and -48 W m^{-2} (**Figure 4a**). The longwave downwelling (LWD) observations range from 116 to 291 W m^{-2} at the sites with highest frequencies at around 155 W m^{-2} and between 200 and 240 W m^{-2} (**Figure 4b**). The MOSAiC sites show differences in frequency and most frequent longwave radiation but, in general, share the same characteristics. Much of the variability among the sites is due to different sample periods, related to intermittent data outages at individual sites. The bimodal distributions are related to the radiative states and, in detail, the radiatively clear state is represented by the frequency peaks at lower values in the LWN and LWD distributions. In the following, we will use the threshold LWN $= -35$ W m^{-2} to identify radiatively clear conditions in the observation record. The respective distributions of LWN and LWD, derived from the ERA5 reanalysis, do not show

a bimodal distribution, instead they are centred at around -30 and 185 W m^{-2}, respectively.

We performed a categorical verification in order to analyze the capability of ERA5 to simulate radiatively clear conditions correctly, defined by the -35 W m^{-2} LWN threshold. In total, as average of all sites, 40.7% of the winter observations are radiatively clear and ERA5 estimates this fraction with a total value of 44.0% of identified radiatively clear events. Furthermore, the verification shows 26.2% of correct simulations (*hits*), 17.7% false simulation of radiatively clear conditions (*false alarms*), and thus 14.5% of the winter, radiatively clear conditions were missed (*misses*), averaged for the sites.

Representation of surface temperature in ERA5
Analysis along the winter 2019/2020 MOSAiC trajectory
Winter MOSAiC trajectory observations of the surface temperature range from $-41°$C to $-5°$C at the sites (Figure S1). Some of the lowest winter temperatures occurred during the clear sky cases CS-1 and CS-2, for the example of L1 with $-37°$C (December 31, 2019) and $-39°$C (February 15, 2020; **Figure 5**). MODIS satellite observations of the surface temperature agree with the MOSAiC observations along the drift trajectory and have a small negative bias of $-1.3°$C, when compared to MOSAiC for all winter radiatively clear conditions and averaged over all sites. The biases at the MOSAiC sites agree in general, except for lower values at L3.

Comparing the ERA5 reanalysis to the MOSAiC observations site mean, the temporal evolution is captured with a Pearson correlation coefficient of 0.8 and RMSE of 4.3°C, during the entire winter 2019/2020. The ERA5 surface temperature has a warm bias of 1.9°C averaged for the winter. The bias is higher during the clear sky event CS-1
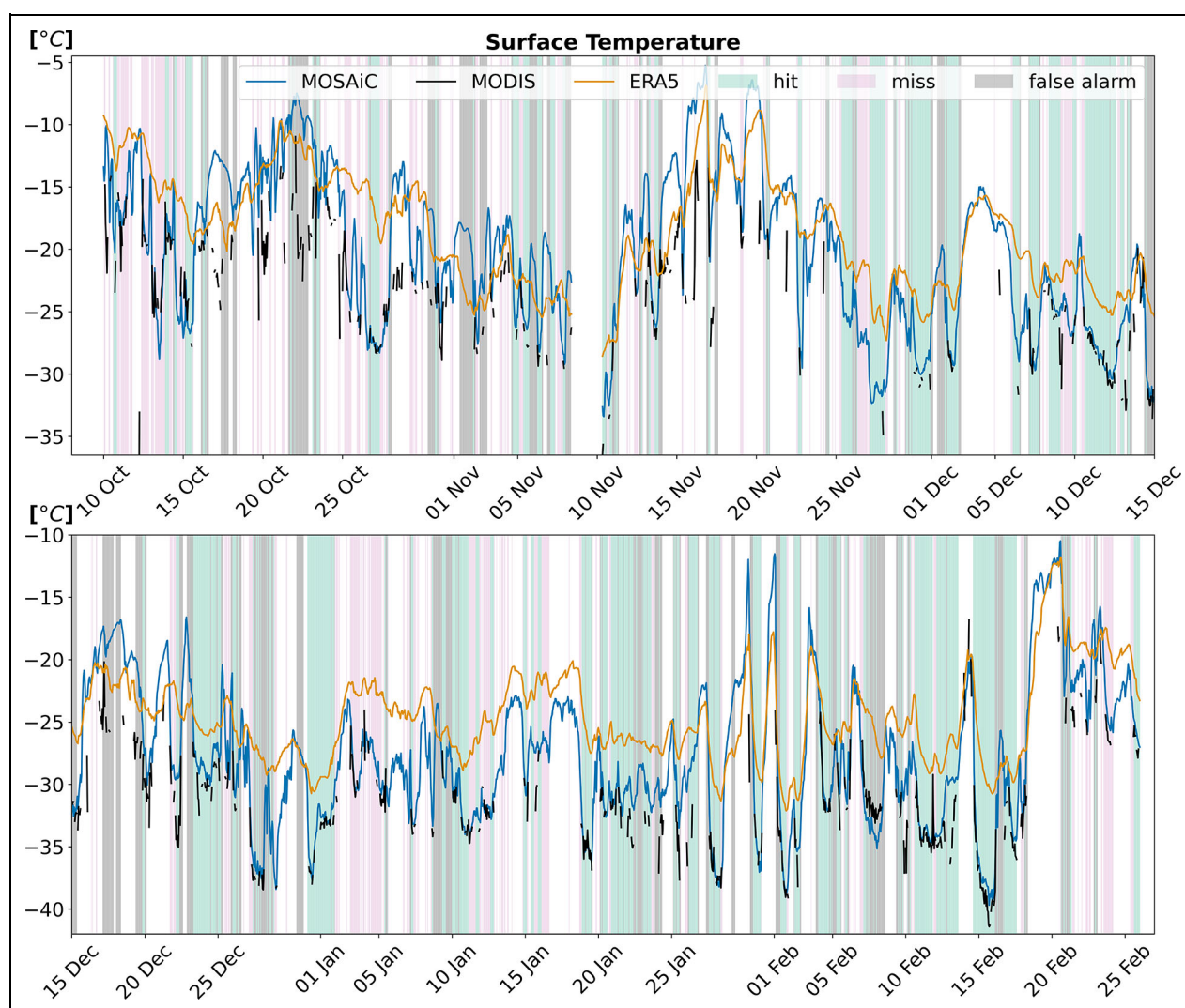
Figure 5. Time series of surface temperature. Surface temperature [°C] along the MOSAiC trajectory of site L1 from October 9, 2019, to February 26, 2020, for MOSAiC observations (blue), MODIS satellite observations (black), and ERA5 reanalysis (orange). *Hits, misses,* and *false alarms* of ERA5 simulating the radiatively clear state according to LWN < −35 W m^{-2} are shown by background coloring (green, red, and gray). MOSAiC = Multidisciplinary drifting Observatory for the Study of Arctic Climate.

with 3.4°C and with 4.3°C–4.6°C during the case CS-2, as well as, when considering all radiatively clear winter conditions (CS) and the ones that where captured by ERA5 (hits; **Table 1**, site mean). The bias computed for the individual stations L1, L2, and Met City is very similar, but L3 shows smaller values reduced by up to 1°C.

Generally, the variability of the surface temperature between each of the observation stations can be estimated by analyzing the respective mean absolute error and RMSE values, separately for MOSAiC, MODIS, and ERA5 (**Figure 2**). L3 shows the largest differences to the other sites for all data sets (**Figure 2a**) with values of up to 1.3°C and 1.8°C, respectively. This is consistent with the L3 station showing the largest mean distance of more than 30 km to L1 and L2. The values for the surface temperature differences between the different locations are significantly smaller in the ERA5 reanalysis but consistently show the largest values for the L3 location for the variability measure with values of up to 0.5°C and 0.4°C, respectively. The

MODIS satellite product shows values closer to the in situ observations and also captures the larger deviations for L3 locations.

We relate LWD and T_s to their respective errors in order to understand a potential conditional bias in these variables, representative for the response of surface temperature to (cloud) radiative forcing from the atmosphere (**Figure 6**). The ERA5 surface temperature errors have a linear relation with the observed LWD with a correlation of 0.79 (**Figure 6a**). Large positive errors occur with the lowest LWD, while large negative errors are found for large LWD values. The negative bias for large values in LWD can be larger than 5°C, for relatively warm surface temperatures above −10°C, while the positive bias for small LWD values is around 5°C–10°C for the coldest surface temperatures of around −35°C. Also, the ERA5 errors of LWD and T_s have a linear relation with a correlation of 0.73 (**Figure 6b**). MODIS also has a considerable large negative bias in conditions when LWD is larger than 220 W m^{-2} (**Figure 6c**).

Table 1. Bias of surface temperature in ERA5 reanalysis along the winter MOSAiC trajectory

Time/ Site	L1 (°C)	L2 (°C)	L3 (°C)	Met City (°C)	Site Mean (°C)
$\Delta T_{s_{MOSAiC}}$					
Winter[a]	2.2	2.3	1.3	2.0	1.9
CS[b]	4.8	4.4	3.8	4.5	4.4
hits[c]	4.7	4.4	3.6	4.5	4.3
CS-1[d]	3.9	3.5	2.8	3.3	3.4
CS-2[e]	4.8	4.5	Na	4.6	4.6
$\Delta T_{s_{MODIS}}$					
CS[b]	6.1	5.9	6.0	6.0	6.0
hits[c]	6.0	5.8	5.8	5.8	5.8
CS-1[d]	4.9	4.8	4.7	4.6	4.7
CS-2[e]	6.9	6.8	Na	7.0	6.9

MOSAiC = Multidisciplinary drifting Observatory for the Study of Arctic Climate; Na = not available.

[a]Winter: October 9, 2019, to February 26, 2020 (MOSAiC).

[b]All situations with radiatively clear conditions during winter[a] (CS).

[c]All situations with radiatively clear conditions during winter[a] that are also captured by ERA5 (hits).

[d]Clear sky case CS-1 (0300 UTC, December 31, 2019, to 0400 UTC, January 2, 2020).

[e]Clear sky case CS-2 (0500 UTC, February 10, 2020, to 1400 UTC, February 17, 2020).

A pan-Arctic analysis

In order to better understand the spatial characteristics of the ERA5 reanalysis surface temperature errors on a pan-Arctic scale, we compare the ERA5 surface temperature against the MODIS level-2 satellite product. During the 2 analyzed clear sky events CS-1 and CS-2, temperatures are low, with values below -36°C in the western Central Arctic (**Figure 7b** and **c**). The same patterns can be found averaged for all radiatively clear conditions in winter 2019/2020 for slightly higher temperatures (**Figure 7a**).

Generally, the sea ice surface temperatures simulated by ERA5 during those radiatively clear conditions are significantly higher than the MODIS observations, however, with similar spatial patterns (**Figure 7d–f**). The error of the ERA5 reanalysis surface temperature, compared to MODIS observations, is inhomogeneous over the Arctic (**Figures 8a** and **b** and **9**). During CS, CS-1, and CS-2, the largest $\Delta T_{s_{MODIS}}$ is found in the western Arctic with values larger than 15°C. In addition, significant regional differences can be seen between CS, CS-1, and CS-2. The regional errors average to a pan-Arctic mean of 3.9°C for CS and up to 5.5°C for the clear sky cases (**Table 2**).

We further include snow depth and sea ice thickness satellite products (**Figure 3**) in our analysis, in order to assess their potential impact on the surface temperature errors. Some of the highest values of the surface temperature error can be found north of the North American continent (**Figure 8c–h**), where sea ice and snow thickness are highest (**Figure 3**). Also, in these areas, the sea ice surface temperatures are lowest (**Figure 7**). In order to assess the impact of the representation of the snow depth and sea ice thickness in the ERA5 system quantitatively, we computed the theoretical errors (Equation 1) caused solely by the snow or sea ice (**Figure 8e–h**) and by their combined effect (**Figure 8c** and **d**).
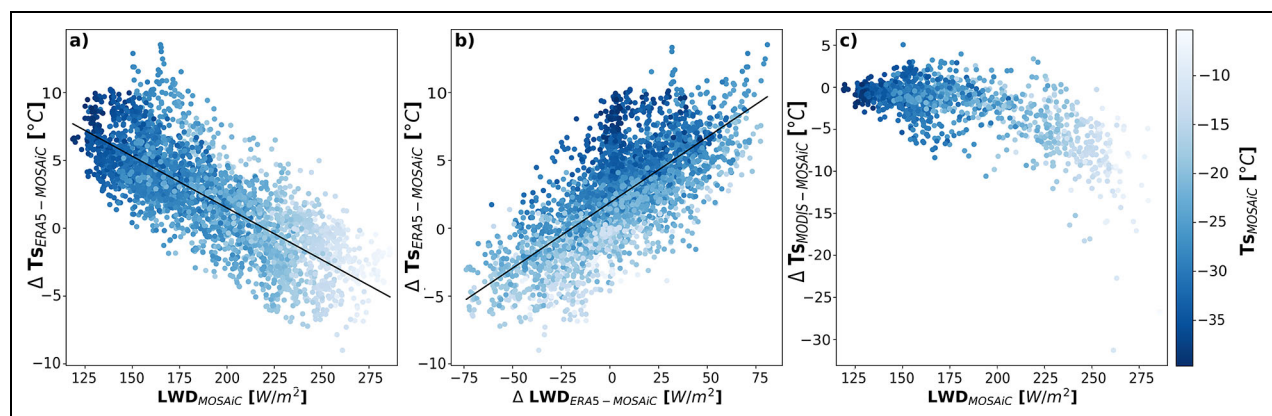
Figure 6. Relation of surface downwelling longwave radiation, the surface temperature, and their errors. Surface downwelling longwave radiation of the MOSAiC observations (*x*-axis in a and c) and error of ERA5 (*x*-axis in b) versus the error of surface temperature comparing ERA5 to MOSAiC (*y*-axis in a and b) and comparing MODIS to MOSAiC (*y*-axis in c). The MOSAiC absolute surface temperature is shown by coloring. Data from the MOSAiC trajectory of site L1 from October 9, 2019, to February 26, 2020. MOSAiC = Multidisciplinary drifting Observatory for the Study of Arctic Climate.
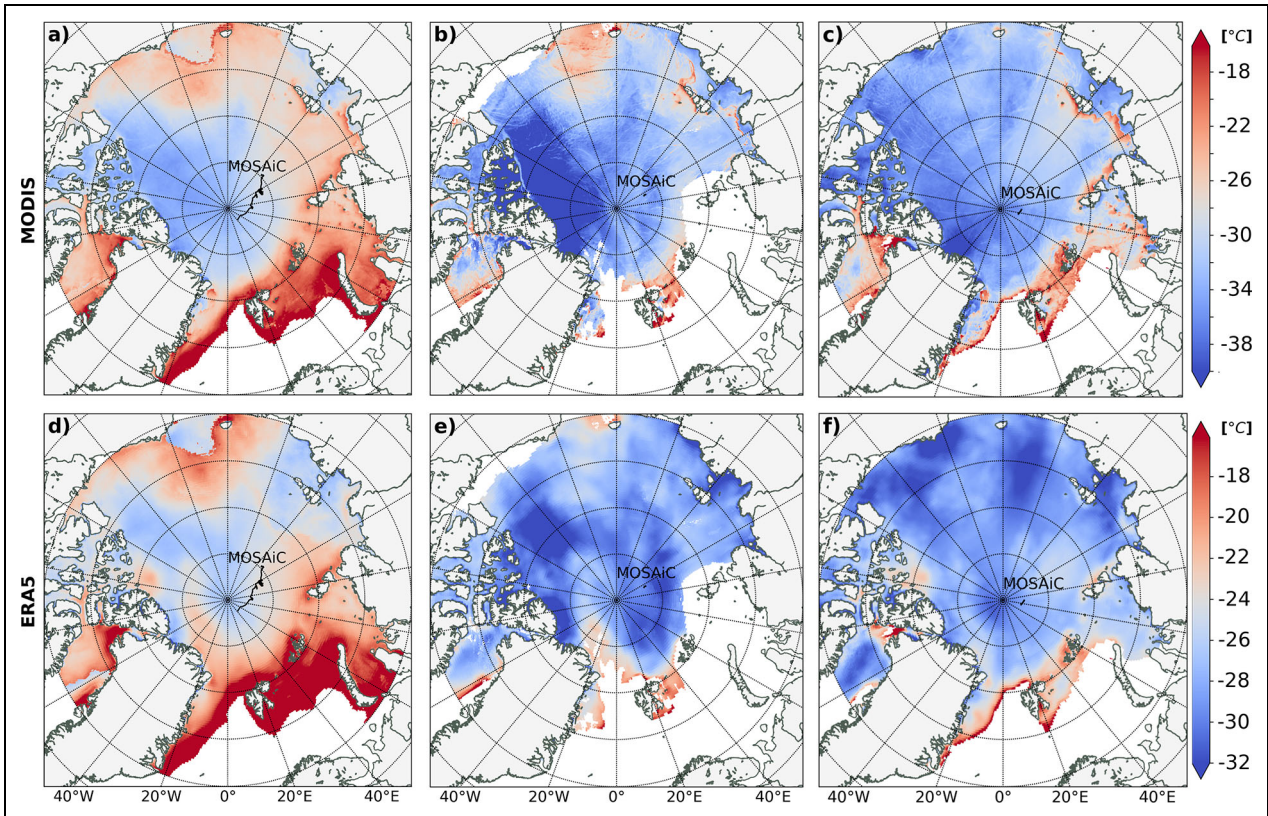
Figure 7. Pan-Arctic surface temperature. Pan-Arctic mean surface temperature [°C] of MODIS (first row) and ERA5 (second row). Averaged for all radiatively clear conditions in winter 2019/2020 (CS; first column) and during clear sky periods CS-1 (second column) and CS-2 (third column). Note the different color bar ranges.

The errors, caused by the misrepresentation of the sea ice thickness ($\Delta T_{s_{theo}:\Delta h_i}$; **Figure 8g** and **h**), show a dipole structure with positive values in the western Central Arctic and negative values in the rest of the sea ice–covered Arctic. The largest cold bias ($> -15°C$) can be found in the areas where the sea ice thickness is close to 1 m, while the warm bias in the western central Arctic is around ($+5°C$).

Surface temperature errors, due to the missing snow layer in the ERA5 system ($\Delta T_{s_{theo}:\Delta hs}$; **Figure 8e** and **f**), show a warm bias across the domain with values up to $+10°C$. The largest values are found in the western Central Arctic, where the observed snow layer is thickest (**Figure 3e** and **f**) and surface temperatures are lowest (**Figure 7**).

The combined theoretical error ($\Delta T_{s_{theo}}$; **Figure 8c** and **d**) shows mostly a warm bias, again, with the largest values in the western Central Arctic ($+12°C$). The error contributions from the missing snow layer $\Delta T_{s_{theo}:\Delta hs}$ and the constant ice thickness $\Delta T_{s_{theo}:\Delta hi}$ tend to compensate each other in some parts of the Arctic but are generally dominated by $\Delta T_{s_{theo}:\Delta hs}$.

The pan-Arctic bias of surface temperature is around 7°C for $T_{s_{theo}}$ and $T_{s_{theo}:\Delta hs}$ and around $-0.7°C$ for $\Delta T_{s_{theo}:\Delta hi}$ (**Table 2**). The spatial characteristics and the pan-Arctic bias are very similar for the 2 clear sky cases, although the errors are slightly higher during CS-1.

In summary, the largest surface temperature errors in the ERA5 reanalysis are found in the western Central Arctic, where sea ice is thickest, snow is deepest, and surface temperatures were low for the analyzed radiatively clear

conditions. While the error estimates agree for this aspect, they show different error magnitudes, with the theoretical error underestimating the actual error. The two clear sky cases show slight differences due to the different meteorological situation at those times.

Discussion

The Arctic winter atmosphere and surface can be divided into 2 dominant states, namely, *radiatively clear* and *opaquely cloudy*. The net and downwelling longwave radiation at the surface (LWN and LWD) are sensitive to the presence of clouds and can serve to identify these 2 radiative states (Zhang et al., 1996; Stramler et al., 2011; Graham et al., 2017; Walden et al., 2017). The analysis of the surface longwave radiative budget during the MOSAiC winter 2019/2020 shows these 2 distinct radiative modes, which are related to the cloudy and clear states of the atmosphere (**Figure 4**). The radiatively clear state can be found with a peak at around -48 W m^{-2} for LWN and at around 155 W m^{-2} for LWD. The opaquely cloudy state has a peak around -7 W m^{-2} for LWN and between 200 and 240 W m^{-2} for LWD. The findings agree for the sites L1, L2, L3, and Met City in general but also show some differences, which could be related to the small-scale variability in cloud coverage (see Figure S1 hits plus misses at the sites) and missing data during the winter at Met City, L2, and L3 (see Methods section).

We find radiatively clear conditions, according to the LWN < -35 W m^{-2} threshold, during 40% of the winter,
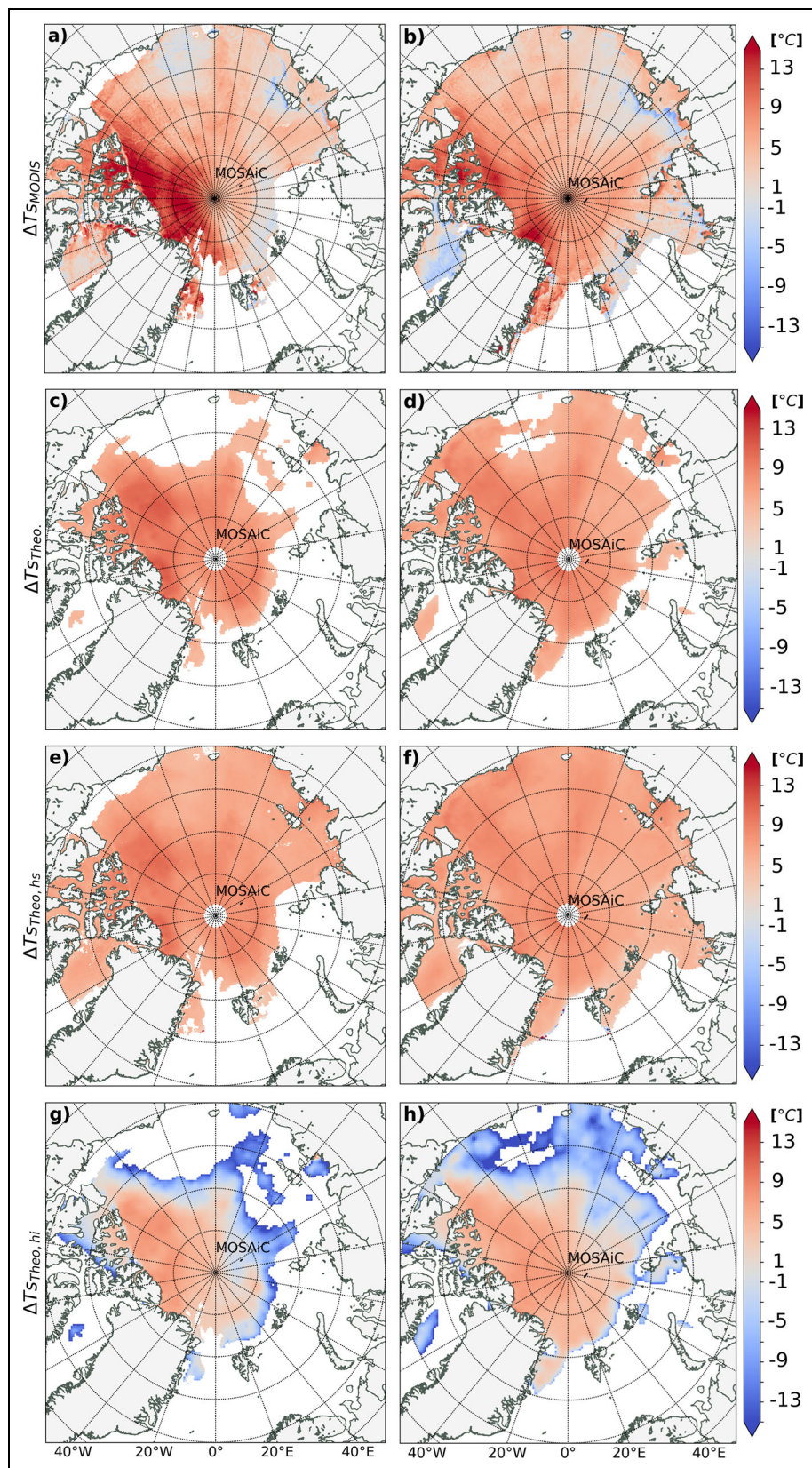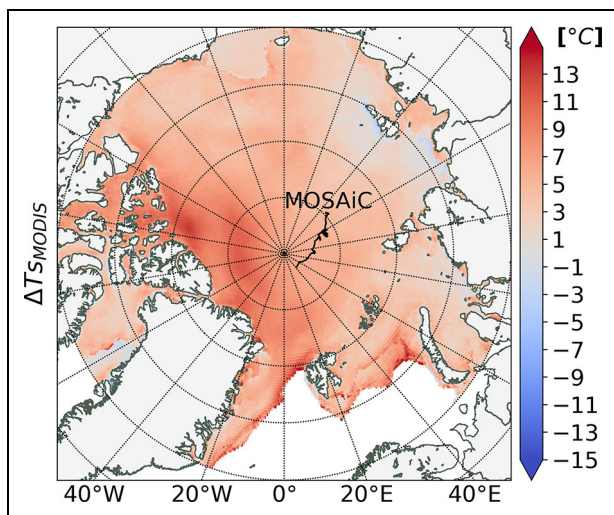
Figure 8. Pan-Arctic surface temperature error during CS-1 and CS-2. Pan-Arctic mean surface temperature error [°C], comparing ERA5 to MODIS (first row) and calculated theoretically (second to fourth row). The theoretical error is based on Equation 1 as described in the Methods section. It is calculated sensitive to the missing snow representation in the model (third row), sensitive to the model sea ice representation (fourth row) and invoking both subsurface representations (second row). The values are averaged for the clear sky periods CS-1 (first column) and CS-2 (second column).

Figure 9. Pan-Arctic surface temperature error during CS. Pan-Arctic mean surface temperature error [°C], comparing ERA5 to MODIS, averaged for all radiatively clear conditions during the winter 2019/2020 (CS).

Table 2. Pan-Arctic bias of surface temperature in ERA5 reanalysis

Error Estimate	CS-1[a] (°C)	CS-2[b] (°C)
$\Delta T_{s_{MODIS}}$	5.5	5.0
$\Delta T_{s_{theo}}$[c]	7.5	6.9
$\Delta T_{s_{theo:\Delta hs}}$[c]	6.9	6.5
$\Delta T_{s_{theo:\Delta h_i}}$[c]	−0.8	−0.6

[a]Clear sky case CS-1 (0300 UTC, December 31, 2019, to 0400 UTC January 2, 2020).

[b]Clear sky case CS-2 (0500 UTC, February 10, 2020, to 1400 UTC, February 17, 2020).

[c]Theoretical biases calculated as described in Methods section and related to **Figure 8c−h**.

highlighting the climatological importance of these conditions. The MODIS cloud mask shows that during the 2 radiatively clear MOSAiC cases, CS-1 and CS-2, there is an overall low cloud coverage on pan-Arctic scales (**Figure 7**). The separation in 2 surface radiative modes can also be found in the data from previous expeditions of Arctic winter (SHEBA and N-ICE), despite the different meteorological conditions (Stramler et al., 2011; Kayser et al., 2017); 66% of the SHEBA winter time conditions were identified as radiatively clear, fulfilling a threshold of LWN < −30 W m^{-2} (Stramler et al., 2011). Other studies used the clear state threshold of LWD < 160 W m^{-2} on N-ICE data (Batrak and Müller, 2019). ERA5 does not reproduce the frequency distribution of the surface longwave radiation along the MOSAiC winter trajectory and, importantly, does not show the bimodal distribution for LWD and LWN (**Figure 4**). This is consistent with the findings of Arduini

et al. (2022) and Graham et al. (2019) for the SHEBA and N-ICE expeditions. The ERA5 reanalysis simulates radiatively clear conditions 44% of the time and simulates 26% correct (*hits*) and 18% incorrect (*false alarm*). It misses radiatively clear conditions 15% of the time (*misses*).

The misrepresentation of the surface radiative energy budget must be approached from different sides. On the one hand, the error in LWN is caused by the overestimated energy flux from ocean, through the sea ice, to the atmosphere. In particular, the insufficient ice and snow representation in ERA5 causes an overestimation of heat conduction through the ice and snow layers (Batrak and Müller, 2019; Arduini et al., 2022). The sea ice representation is further impacted by errors in sea ice concentration (Renfrew et al., 2021) and possibly also by the prescribed constant sea ice conductivity (ECMWF, 2016). More problems can be found in the simulation of turbulent heat fluxes over sea ice (Graham et al., 2019). On the other hand, ERA5 can overestimate the LWD due to cloud property misrepresentation. In addition, surface-based inversions (and their coupling to the surface radiative flux) are not represented well, especially in stable, cold conditions, when the influence of the overestimated heat conduction through ice and snow is highest (Graham et al., 2019; Arduini et al., 2022). This causes errors in the representation of the radiatively clear state and a warm bias of surface temperature.

The analysis of the surface temperature during the MOSAiC winter period showed the lowest surface temperatures during radiatively clear periods, for example, T_s = −39°C on February 15, 2020 (**Figure 5**). On pan-Arctic scales and during the analyzed radiatively clear periods, the lowest surface temperatures are observed in the western half of the Arctic (**Figure 7**). Highest surface temperatures along the winter MOSAiC trajectory occur during storms, as they bring heat and moisture from lower latitudes, causing a smaller negative radiative energy budget (**Figure 5**; Rinke et al., 2021). On pan-Arctic scales, the highest surface temperatures during clear sky conditions are visible toward the marginal ice zones, especially toward the Atlantic Ocean (**Figures 3** and **7**).

Error estimates of the surface temperature are calculated by comparing ERA5 to MOSAiC and MODIS along the trajectory, as well as, comparing to MODIS on a pan-Arctic scale. Compared against the MOSAiC observations, ERA5 captures the general temporal evolution of the surface temperature with a Pearson correlation coefficient of 0.8 and an RMSE of 4.3°C. During radiatively clear conditions, ERA5 has a positive surface temperature error ($\Delta T_{s_{MOSAiC}}$) along the winter MOSAiC trajectory and, as well, in most parts of the Arctic when compared against MODIS (**Figures 5**, **8**, and **9** and **Tables 1** and **2**). The overall ERA5 surface temperature bias along the MOSAiC trajectory for the winter 2019/2020 is around 2°C, while when averaging only over radiatively clear conditions in the same time period, the bias is larger with a value of 4°C (**Table 1**). This is consistent with the findings of a 5°C–15°C surface temperature error by Batrak and Müller (2019), comparing ERA5 to the radiatively clear N-ICE

winter observation data. Interestingly, the bias of all winter radiatively clear conditions (CS) and those captured by ERA5 (hits) are very similar. Occasionally, the surface temperature error can be significantly higher during radiatively clear conditions with very low surface temperatures, which is, for example, the case on February 15, 2020, with an error in the ERA5 surface temperature of about 12°C (**Figure 5**).

The pan-Arctic surface temperature bias of ERA5 when compared to MODIS satellite observation ($\Delta T_{s_{theo}}$) is in the range of -5°C to 15°C (**Figures 8a** and **b** and **9**). Only data points that are identified as radiatively clear conditions are used in the Arctic analysis (see Methods section). It is important to note that the MODIS surface temperatures, which were mainly used for the pan-Arctic assessment, have a cold bias of around 1°C relative to the MOSAiC surface observations in radiatively clear conditions, agreeing with findings in Hall et al. (2004). In addition, our analysis shows that MODIS can have a considerably larger negative bias in conditions with LWD larger than about 220 W m^{-2} (**Figure 6c**), which however should not strongly impact our results since MODIS data have only been used for the comparison in conditions of LWN -35 W m^{-2} as simulated by ERA5.

The ERA5 model system does not include a snow model on top of the sea ice, also sea ice thickness is not a prognostic variable, and is set to a constant value of 1.5 m. Due to the importance of the snow-ice layer in insulating the cold atmosphere from the ocean (Overland and Guest, 1991), the simplified representation in ERA5 causes large errors, specifically when the atmosphere is very cold, the snow-depth is large O(0.1 m) or the sea ice thickness significantly deviates from 1.5 m (Batrak and Müller, 2019). In the present study, we analyzed the separate, as well as the combined, impacts of ERA5's snow-depth and sea ice thickness error in the surface temperature. For this analysis, we used satellite products of snow-depth (AMSR-E/2) and sea ice thickness (CryoSat/SMOS). The retrieval methods for those products are subject to a number of uncertainties, including the interdependency between the snow depth and sea ice thickness retrievals (Ricker et al., 2017; Rostosky et al., 2018). CryoSat sea ice thickness, having most influence in the CryoSat/SMOS product for the Central Arctic, was assigned an uncertainty of 0.5–0.7 m for the winter at the MOSAiC CO. AMSR-E/2 snow depth showed good agreement with the MOSAiC in situ observations within 5 cm uncertainty (Krumpen et al., 2021). Assuming conditions, typical for late winter radiatively clear periods at MOSAiC, with $T_s = -40$°C, $h_i = 2$ m, and $h_s = 0.2$ m, the above uncertainties would yield an error of 2°C. It is important to note that the equation used to estimate the theoretical errors is based on a first-order approximation of the surface energy budget and thus could partly only be applied on areas with $h_i \geq 1$ m. Also, it excludes errors in the turbulent heat fluxes (Batrak and Müller, 2019).

We find that the missing snow layer can indeed explain the general warm bias in the sea ice surface temperature in ERA5 during winter radiatively clear events. The general pattern, as well as magnitude of $\Delta T_{s_{Theo}}$, snow depth, and

sea ice are consistent (**Figures 3** and **8c–h**). The combined theoretical error is in the range of 5°C–12°C (**Figure 8c** and **d**). However, the separate treatment of snow depth and sea ice thickness as error sources also shows that in areas where the sea ice thickness is significantly below 1.5 m, the error caused by the missing snow-layer (warm bias O(6°C)) is compensated by the error caused by the underestimation of the sea ice thickness (cold bias O(-4°C); **Figure 8e–h**). Due to the higher insulation effect of snow (the conductivity of snow is about 7 times smaller than that of sea ice), the influence of the missing snow layer dominates the error in most regions, and thus, the combined temperature error is mostly positive (**Figure 8c** and **d**). Thus, the pan-Arctic mean for the theoretical combined error is around 7°C, agreeing reasonably well with the respective mean $\Delta T_{s_{MODIS, Arctic}} \approx 5$°C (**Table 2**). Regional and pan-Arctic differences of $\Delta T_{s_{MODIS}}$ and the $\Delta T_{s_{theo.}}$ derived from the sea ice and snow thickness misrepresentation as only error source in $\Delta T_{s_{theo.}}$, compared to the actual error $\Delta T_{s_{MODIS}}$, including also other possible error sources explained above.

The misrepresentation of snow and sea ice layers in the ERA5 system has its major impact when the surface temperature is low relative to the ocean surface temperature of around -2°C. In other words, the conductive heat flux from ocean to atmosphere, and thus the snow and sea ice representation, is most relevant when the atmosphere–ocean temperature difference is large (see also Equation 1). This is generally the case for radiatively clear conditions. Thus, it is essential to study the Arctic system in this state. The importance of the low absolute temperature can also be seen by comparing the two case studies on a pan-Arctic scale. The lower absolute surface temperatures in CS-1 cause higher ΔT_s although the errors in the sea ice thickness and snow layer depth are larger in CS-2 (**Figures 3**, **7**, and **8**).

Generally, our analysis shows that the ERA5 surface temperature has a conditional error depending on the LWD, representative for the radiative state of the atmosphere, and the absolute surface temperature (**Figure 6a**). The error is positive for low LWD values (radiatively clear conditions) and becomes negative for large LWD values (cloudy state). In cloudy conditions, the temperatures are usually closer to the freezing point, and thus, the effect of deficiencies in the snow depth and sea ice thickness on the surface temperature becomes smaller. Insufficient sea ice and snow representation in ERA5 can still have an effect due to the decreased response to rapid ambient temperature changes (Arduini et al., 2022). The comparison of observed LWD during MOSAiC and the one simulated by ERA5 shows that in connection to the cold bias, LWD is underestimated in the model (**Figure 6b**). Hence, other deficiencies in the model system must be dominant in opaquely cloudy conditions with a negative impact on the representation of the downwelling radiation and surface radiative energy budget.

The multiple observation sites at MOSAiC with distances ranging from 11 to 34 km gives us insights into the spatial variability of surface temperature. Mean absolute differences of surface temperature between the 4

stations range between 0.6°C and 1.3°C. This spatial variability can be considered subgrid scale for ERA5 and thus is not captured (0.1°C–0.4°C). The MODIS level 2 satellite product with a grid resolution of 5 km represents a variability of surface temperature similar to that of the 4 observation sites at MOSAiC. In addition, to the spatial variability of the surface temperature, the analyzed MOSAiC sites L1, L2, L3, and Met City have different sea ice and snow characteristics. The theoretical error calculations are based on the pan-Arctic snow depth and sea ice thickness products with resolution of 5 and 31 km, respectively, and thus representing regional mean ice and snow layer thickness, and not representing the interstation variability of the MOSAiC network.

Summary and conclusion

The MOSAiC winter surface radiative energy budget is predominantly found in the radiatively clear and the opaquely cloudy states, which are, however, not distinguishable in the ERA5 reanalysis. Radiatively clear conditions can be identified in ERA5 output along the MOSAiC trajectory, despite the missing state separation in the surface radiation budget.

The surface temperature on Arctic sea ice is strongly connected to the atmospheric radiative states. Temperature values reach down to −40°C during radiatively clear conditions and are closer to 0°C during the cloudy state. In connection to the deficiencies in the surface radiative budget, the extreme temperature values are not captured and a warm bias of 2°C was discovered for the October to February MOSAiC trajectory. During radiatively clear conditions, the bias is large with an average of 4°C when compared to MOSAiC observations and of −5°C to 15°C on regional Arctic scales. Regional errors in the surface temperature are highest where the sea ice and snow layer is thick and during events with very low surface temperatures. It is shown that during radiatively clear conditions, a large part of the deficiencies in the surface radiative energy budget and surface temperature are caused by insufficient representation of ice thickness and snow depth. This is consistent with Batrak and Müller (2019), who showed that during radiatively clear conditions, the conductive heat flux through the ice-snow layer is overestimated in the reanalyses by about 30–40 W m^{-2} and compensated by an increased outgoing longwave radiation and thus increased surface temperature. The representation of the ice thickness in ERA5 with a constant value of 1.5 m results in a cold surface temperature bias in areas where the real ice thickness is significantly smaller. This error can be as large as −15°C. However, this cold bias is compensated by the generally warm bias across the entire Arctic caused by the missing snow layer in the ERA5 reanalysis system. The influence of the insufficient snow and sea ice representation is most effective during the coldest surface temperatures and thus radiatively clear conditions. Modeling snow on Arctic sea ice would improve the representation of the Arctic winter states, and especially in cold radiatively clear conditions, the representation of surface temperature and boundary layer stability (Arduini et al., 2022). In opaquely cloudy conditions,

a cold bias, which can be larger than 5°C, is visible in the data and shows that other error sources in the ERA5 model system have a significant impact on the surface radiative energy budget. The results must be viewed in the light of uncertain satellite observations.

This study could be further extended with snow and sea ice observations from the MOSAiC drift campaign (Nicolaus et al., 2022) and through analysis of surface temperature biases in opaquely cloudy periods and during polar day. Error sources in the ERA5 reanalysis could be analyzed in even more detail in future studies, such as the simulation of boundary layer stability, turbulent heat fluxes, and cloud properties (Graham et al., 2017; Kayser et al., 2017; Graham et al., 2019; Arduini et al., 2022). MOSAiC measurements are available for such analyses, including, meteorological radiosonde observations and ASFS measurements of the surface momentum flux and near-surface meteorology (Shupe et al., 2022). In addition, errors caused by insufficient representation of sea ice concentration (Renfrew et al., 2021) could be evaluated with MOSAiC data from June to mid-August 2020, when the ship Polarstern drifted through the Fram Strait amid disintegrating sea ice floes.

Data accessibility statement

Met City and ASFS data are available from the Arctic Data Center (Cox et al., 2021a; Cox et al., 2021b; Cox et al., 2021c; Cox et al., 2021d). The ERA5, CryoSat-2/SMOS, and OSI-SAF data are available from the Copernicus Climate Change Service Climate Data Store (https://cds.climate.copernicus.eu/). The MODIS satellite retrieval is available through NASA's dissemination server (https://modis.gsfc.nasa.gov). The AMSR-2 snow depth product is available at https://seaice.uni-bremen.de/data/amsr2/SnowDepth/n25000/.

Supplemental files

The supplemental files for this article can be found as follows:

Figure S1. Time series of surface temperature for all sites. Surface temperature [°C] along the MOSAiC trajectory of sites L1 (a), L2 (b), L3 (c) andMetCity (d) from October 9, 2019, to February 26, 2020, for MOSAiC observations (blue), MODIS satellite observation (black) and ERA5 reanalysis (orange). Hits, misses and false alarms of ERA5 simulating the radiatively clear state according to LWN < −35 W m^{-2} are shown by background coloring (green, red, grey).

Acknowledgments

Program. The authors would like to thank Yurii Batrak for providing a merged hourly MODIS surface temperature data set. They are grateful to Annette Rinke and Nikki Vercauteren for their valuable discussions.

Competing interests

The authors declare that they have no competing interests.

Author contributions

Contribution to the conception and design: LH, MM.
Contribution to the acquisition of data: MDS, PR.
Contribution to analysis and interpretation of data: LH, MM.
Draft and/or revision of the article: All authors.
Final approval of the version to be published: All authors.

References

Arduini, G, **Keeley, S**, **Day, JJ**, **Sandu, I**, **Zampieri, L**, **Balsamo, G.** 2022. On the importance of representing snow over sea-ice for simulating the Arctic boundary layer. *Journal of Advances in Modeling Earth Systems* **14**(7): e2021MS002777. DOI: http://dx.doi.org/10.1029/2021MS002777.

Batrak, Y, **Müller, M.** 2019. On the warm bias in atmospheric reanalyses induced by the missing snow over Arctic sea-ice. *Nature Communications* **10**: 4170. DOI: http://dx.doi.org/10.1038/s41467-019-11975-3.

Cohen, L, **Hudson, SR**, **Walden, VP**, **Graham, RM**, **Granskog, MA.** 2017. Meteorological conditions in a thinner Arctic sea ice regime from winter to summer during the Norwegian Young Sea Ice expedition (N-ICE2015). *Journal of Geophysical Research: Atmospheres* **122**(14): 7235–7259. DOI: http://dx.doi.org/10.1002/2016JD026034.

Cox, C, **Gallagher, M**, **Shupe, M**, **Persson, O**, **Solomon, A**, **Ayers, T**, **Costa, D**, **Hutchings, J**, **Leach, J**, **Morris, S**, **Osborn, J.** 2021a. Atmospheric Surface Flux Station #30 measurements (Level 2, Version 3), Multidisciplinary Drifting Observatory for the Study of Arctic Climate (MOSAiC), central Arctic, October 2019–September 2020. Arctic Data Center. DOI: http://dx.doi.org/10.18739/A20C4SM1J.

Cox, C, **Gallagher, M**, **Shupe, M**, **Persson, O**, **Solomon, A**, **Ayers, T**, **Costa, D**, **Hutchings, J**, **Leach, J**, **Morris, S**, **Osborn, J**, **Pezoa, S**, **Uttal, T.** 2021b. Atmospheric Surface Flux Station #40 measurements (Level 2, Version 3), Multidisciplinary Drifting Observatory for the Study of Arctic Climate (MOSAiC), central Arctic, October 2019–September 2020. Arctic Data Center. DOI: http://dx.doi.org/10.18739/A2CJ87M7G.

Cox, C, **Gallagher, M**, **Shupe, M**, **Persson, O**, **Solomon, A**, **Ayers, T**, **Costa, D**, **Hutchings, J**, **Leach, J**, **Morris, S**, **Osborn, J**, **Pezoa, S**, **Uttal, T.** 2021c. Atmospheric Surface Flux Station #50 measurements (Level 2, Version 3), Multidisciplinary Drifting Observatory for the Study of Arctic Climate (MOSAiC), central Arctic, October 2019–September 2020. Arctic Data Center. DOI: http://dx.doi.org/10.18739/A2445HD46.

Cox, C, **Gallagher, M**, **Shupe, M**, **Persson, O**, **Solomon, A**, **Blomquist, B**, **Brooks, I**, **Costa, D**, **Gottas, D**, **Hutchings, J**, **Osborn, J**. 2021d. 10-meter (m) meteorological flux tower measurements (Level 1 Raw), Multidisciplinary Drifting Observatory for the Study of Arctic Climate (MOSAiC), central Arctic, October 2019–September 2020. Arctic Data Center. DOI: http://dx.doi.org/10.18739/A2VM42Z5F.

European Centre for Medium-Range Weather Forecasts. 2016. IFS documentation CY41R2—Part IV: Physical processes, in *IFS documentation CY41R2*. Reading, UK: European Centre for Medium-Range Weather Forecasts (IFS Documentation 4). DOI: http://dx.doi.org/10.21957/tr5rv27xu.

Graham, RM, **Cohen, L**, **Ritzhaupt, N**, **Segger, B**, **Graversen, RG**, **Rinke, A**, **Walden, VP**, **Granskog, MA**, **Hudson, SR.** 2019. Evaluation of six atmospheric reanalyses over Arctic sea ice from winter to early summer. *Journal of Climate* **32**(14): 4121–4143. DOI: http://dx.doi.org/10.1175/JCLI-D-18-0643.1.

Graham, RM, **Rinke, A**, **Cohen, L**, **Hudson, SR**, **Walden, VP**, **Granskog, MA**, **Dorn, W**, **Kayser, M**, **Maturilli, M.** 2017. A comparison of the two Arctic atmospheric winter states observed during N-ICE2015 and SHEBA. *Journal of Geophysical Research: Atmospheres* **122**(11): 5716–5737. DOI: http://dx.doi.org/10.1002/2016JD025475.

Hall, DK, **Key, J**, **Casey, K**, **Riggs, G**, **Cavalieri, D.** 2004. Sea ice surface temperature product from MODIS. *IEEE Transactions on Geoscience and Remote Sensing* **42**(5): 1076–1087. DOI: http://dx.doi.org/10.1109/TGRS.2004.825587.

Hall, DK, **Riggs, G.** 2015. *MODIS/Aqua sea ice extent 5-min L2 Swath 1km, Version 6—USER GUIDE.* Boulder, CO: National Aeronautics and Space Administration, NASA and National Snow and Ice Data Center NSIDC. DOI: http://dx.doi.org/10.5067/MODIS/MYD29.006.

Hersbach, H, **Bell, B**, **Berrisford, P**, **Hirahara, S**, **Horányi, A**, **Muñoz-Sabater, J**, **Nicolas, J**, **Peubey, C**, **Radu, R**, **Schepers, D**, **Simmons, A**, **Soci, C**, **Abdalla, S**, **Abellan, X**, **Balsamo, G**, **Bechtold, P**, **Biavati, G**, **Bidlot, J**, **Bonavita, M**, **De Chiara, G**, **Dahlgren, P**, **Dee, D**, **Diamantakis, M**, **Dragani, R**, **Flemming, J**, **Forbes, R**, **Fuentes, M**, **Geer, A**,

Haimberger, L, Healy, S, Hogan, RJ, Hólm, E, Janisková, M, Keeley, S, Laloyaux, P, Lopez, P, Lupu, C, Radnoti, G, de Rosnay, P, Rozum, I, Vamborg, F, Villaume, S, Thépaut, J-N. 2020. The ERA5 global reanalysis. *Quarterly Journal of the Royal Meteorological Society* **146**(730): 1999–2049. DOI: http://dx.doi.org/10.1002/qj.3803.

Jakobson, E, Vihma, T, Palo, T, Jakobson, L, Keernik, H, Jaagus, J. 2012. Validation of atmospheric reanalyses over the central Arctic Ocean. *Geophysical Research Letters* **39**(10). DOI: http://dx.doi.org/10.1029/2012GL051591.

Kayser, M, Maturilli, M, Graham, RM, Hudson, SR, Rinke, A, Cohen, L, Kim, J-H, Park, S-J, Moon, W, Granskog, MA. 2017. Vertical thermodynamic structure of the troposphere during the Norwegian young sea ICE expedition (N-ICE2015). *Journal of Geophysical Research: Atmospheres* **122**(20): 10855–10872. DOI: http://dx.doi.org/10.1002/2016JD026089.

Knust, R. 2017. Polar research and supply vessel POLARSTERN operated by the Alfred-Wegener-Institute. *Journal of Large-scale Research Facilities* **3**: A119. DOI: http://dx.doi.org/10.17815/jlsrf-3-163.

Krumpen, T, von Albedyll, L, Goessling, HF, Hendricks, S, Juhls, B, Spreen, G, Willmes, S, Belter, HJ, Dethloff, K, Haas, C, Kaleschke, L. 2021. MOSAiC drift expedition from October 2019 to July 2020: Sea ice conditions from space and comparison with previous years. *The Cryosphere* **15**(8): 3897–3920. DOI: http://dx.doi.org/10.5194/tc-15-3897-2021.

Lindsay, R, Wensnahan, M, Schweiger, A, Zhang, J. 2014. Evaluation of seven different atmospheric reanalysis products in the Arctic. *Journal of Climate* **27**(7): 2588–2606. DOI: http://dx.doi.org/10.1175/JCLI-D-13-00014.1.

Nicolaus, M, Perovich, DK, Spreen, G, Granskog, MA, von Albedyll, L, Angelopoulos, M, Anhaus, P, Arndt, S, Belter, HJ, Bessonov, V, Birnbaum, G. 2022. Overview of the MOSAiC expedition: Snow and sea ice. *Elementa: Science of the Anthropocene* **10**(1): 000046. DOI: http://dx.doi.org/10.1525/elementa.2021.000046.

Overland, JE, Guest, PS. 1991. The Arctic snow and air temperature budget over sea ice during winter. *Journal of Geophysical Research: Oceans* **96**(C3): 4651–4662. DOI: http://dx.doi.org/10.1029/90JC02264.

Peixoto, JP, Oort, AH. 1992. Physics of climate. *Bulletin of the American Meteorological Society* **73**(11). Available at https://www.osti.gov/biblio/7287064.

Renfrew, IA, Barrell, C, Elvidge, AD, Brooke, JK, Duscha, C, King, JC, Kristiansen, J, Cope, TL, Moore, GW, Pickart, RS, Reuder, J. 2021. An evaluation of surface meteorology and fluxes over the Iceland and Greenland Seas in ERA5 reanalysis: The impact of sea ice distribution. *Quarterly Journal of the Royal Meteorological Society* **147**(734): 691–712. DOI: http://dx.doi.org/10.1002/qj.3941.

Ricker, R, Hendricks, S, Kaleschke, L, Tian-Kunze, X, King, J, Haas, C. 2017. A weekly Arctic sea-ice thickness data record from merged CryoSat-2 and SMOS satellite data. *The Cryosphere* **11**(4): 1607–1623. DOI: http://dx.doi.org/10.5194/tc-11-1607-2017.

Rinke, A, Cassano, JJ, Cassano, EN, Jaiser, R, Handorf, D. 2021. Meteorological conditions during the MOSAiC expedition: Normal or anomalous? *Elementa: Science of the Anthropocene* **9**(1): 00023. DOI: http://dx.doi.org/10.1525/elementa.2021.00023.

Rostosky, P, Spreen, G, Farrell, SL, Frost, T, Heygster, G, Melsheimer, C. 2018. Snow depth retrieval on Arctic sea ice from passive microwave radiometers—Improvements and extensions to multiyear ice using lower frequencies. *Journal of Geophysical Research: Oceans* **123**(10): 7120–7138. DOI: http://dx.doi.org/10.1029/2018JC014028.

Serreze, MC, Barry, RG. 2014. The basic atmospheric and ocean energy budgets, in *The Arctic climate system*. 2nd ed. Cambridge, UK: Cambridge University Press: 65–84. (Cambridge Atmospheric and Space Science Series). DOI: http://dx.doi.org/10.1017/CBO9781139583817.006.

Shupe, M, Rex, M, Blomquist, B, Persson, POG, Schmale, J, Uttal, T, Althausen, D, Angot, H, Archer, S, Bariteau, L, Beck, I, Bilberry, J, Bucci, S, Buck, C, Boyer, M, Brasseur, Z, Brooks, IM, Calmer, R, Cassano, J, Castro, V, Chu, D, Costa, D, Cox, CJ, Creamean, J, Crewell, S, Dahlke, S, Damm, E, de Boer, G, Deckelmann, H, Dethloff, K, Dütsch, M, Ebell, K, Ehrlich, A, Ellis, J, Engelmann, R, Fong, AA, Frey, MM, Gallagher, MR, Ganzeveld, L, Gradinger, R, Graeser, J, Greenamyer, V, Griesche, H, Griffiths, S, Hamilton, J, Heinemann, G, Helmig, D, Herber, A, Heuzé, C, Hofer, J, Houchens, T, Howard, D, Inoue, J, Jacobi, H-W, Jaiser, R, Jokinen, T, Jourdan, O, Jozef, G, King, W, Kirchgaessner, A, Klingebiel, M, Krassovski, M, Krumpen, T, Lampert, A, Landing, W, Laurila, T, Lawrence, D, Lonardi, M, Loose, B, Lüpkes, C, Maahn, M, Macke, A, Maslowski, W, Marsay, C, Maturilli, M, Mech, M, Morris, S, Moser, M, Nicolaus, M, Ortega, P, Osborn, J, Pätzold, F, Perovich, DK, Petäjä, T, Pilz, C, Pirazzini, R, Posman, K, Powers, H, Pratt, KA, Preußer, A, Quéléver, L, Radenz, M, Rabe, B, Rinke, A, Sachs, T, Schulz, A, Siebert, H, Silva, T, Solomon, A, Sommerfeld, A, Spreen, G, Stephens, M, Stohl, A, Svensson, G, Uin, J, Viegas, J, Voigt, C, von der Gathen, P, Wehner, B, Welker, JM, Wendisch, M, Werner, M, Xie, Z, Yue, F. 2022. Overview of the MOSAiC expedition: Atmosphere. *Elementa: Science of the Anthropocene* **10**(1): 00060. DOI: http://dx.doi.org/10.1525/elementa.2021.00060.

Shupe, M, Rex, M, Dethloff, K, Damm, E, Fong, AA, Gradinger, R, Heuze, C, Loose, B, Makarov, A, Maslowski, W, Nicolaus, M, Perovich, D, Rabe, B, Rinke, A, Sokolov, V, Sommerfeld, A. 2020. Arctic Report Card 2020: The MOSAiC expedition:

A year drifting with the Arctic sea ice. DOI: http://dx.doi.org/10.25923/9g3v-xh92.

Shupe, MD, Intrieri, JM. 2004. Cloud radiative forcing of the Arctic surface: The influence of cloud properties, surface albedo, and solar zenith angle. *Journal of Climate* **17**(3): 616–628. DOI: http://dx.doi.org/10.1175/1520-0442(2004)017<0616:CRFOTA>2.0.CO;2.

Sorteberg, A, Kattsov, V, Walsh, JE, Pavlova, T. 2007. The Arctic surface energy budget as simulated with the IPCC AR4 AOGCMs. *Climate Dynamics* **29**: 131–156. DOI: http://dx.doi.org/10.1007/s00382-006-0222-9.

Stramler, K, Genio, ADD, Rossow, WB. 2011. Synoptically driven Arctic winter states. *Journal of Climate* **24**(6): 1747–1762. DOI: http://dx.doi.org/10.1175/2010JCLI3817.1.

Tjernström, M, Graversen, RG. 2009. The vertical structure of the lower Arctic troposphere analysed from observations and the ERA-40 reanalysis. *Quarterly Journal of the Royal Meteorological Society* **135**(639): 431–443. DOI: http://dx.doi.org/10.1002/qj.380.

Uttal, T, Curry, JA, McPhee, MG, Perovich, DK, Moritz, RE, Maslanik, JA, Guest, PS, Stern, HL, Moore, JA, Turenne, R, Heiberg, A, Serreze, MC, Wylie, DP, Persson, OG, Paulson, CA, Halle, C, Morison, JH, Wheeler, PA, Makshtas, A, Welch, H, Shupe, MD, Intrieri, JM, Stamnes, K, Lindsey, RW, Pinkel, R, Pegau, WS, Stanton, TP, Grenfeld, TC. 2002. Surface heat budget of the Arctic Ocean. *Bulletin of the American Meteorological Society* **83**(2): 255–276. DOI: http://dx.doi.org/10.1175/1520-0477(2002)083<0255:SHBOTA>2.3.CO;2.

Walden, VP, Hudson, SR, Cohen, L, Murphy, SY, Granskog, MA. 2017. Atmospheric components of the surface energy budget over young sea ice: Results from the N-ICE2015 campaign. *Journal of Geophysical Research: Atmospheres* **122**(16): 8427–8446. DOI: http://dx.doi.org/10.1002/2016JD026091.

Wang, C, Graham, RM, Wang, K, Gerland, S, Granskog, MA. 2019. Comparison of ERA5 and ERA-Interim near-surface air temperature, snowfall and precipitation over Arctic sea ice: Effects on sea ice thermodynamics and evolution. *The Cryosphere* **13**(6): 1661–1679. DOI: http://dx.doi.org/10.5194/tc-13-1661-2019.

Zhang, T, Stamnes, K, Bowling, SA. 1996. Impact of clouds on surface radiative fluxes and snowmelt in the Arctic and subarctic. *Journal of Climate* **9**(9): 2110–2123. DOI: http://dx.doi.org/10.1175/1520-0442(1996)009<2110:IOCOSR>2.0.CO;2.